Received: 21 August 2020 | Revised: 28 September 2020 | Accepted: 3 February 2021

DOI: 10.1002/int.22386

RESEARCH ARTICLE

WILEY

Organic solar cells defects classification by using a new feature extraction algorithm and an EBNN with an innovative pruning algorithm

Grazia Lo Sciuto[1] | Giacomo Capizzi[1] | Rafi Shikler[2] | Christian Napoli[3]

[1]Department of Electrical Electronics and Informatics Engineering, University of Catania, Catania, Italy

[2]Department of Electrical and Computer Engineering, Ben-Gurion University of the Negev, Beer-Sheva, Israel

[3]Department of Computer, Automation and Management Engineering, Sapienza University of Rome, Rome, Italy

Correspondence
Christian Napoli, Department of Computer, Automation and Management Engineering, Sapienza University of Rome, Rome 00135, Italy.
Email: cnapoli@diag.uniroma1.it

Abstract

Physical defects reduce the organic solar cells (OSC) functioning. Throughout the OSC fabrication process, the defects can occur, for instance, by scratches or uneven morphologies. In general, bulk defects, interface defects, and interconnect defects can promote shunt and series resistance of the cell. It is crucial to properly detect and classify such defects and their amount in the structure. Correlating such defects with the performance of the cell is important both during the R&D stages to optimize processes, and for mass production stages where defects detection is an integral part of the production line. For the recognition of texture variations in the scanning electron microscope images caused by these defects is crucial the definition of a set of features for texture representation. Because the low-order Zernike moments can represent the whole shape of the image and the high-order Zernike moments can describe the detail. Then, in our case, the feature of the image can be represented by a small number of Zernike moments. In fact, the feature set extracted and described by the Zernike moments are not sensitive to the noises and are hardly redundant. So it possible concentrate the signal energy over a set of few vectors. Finally, for classification, an elliptical basis function neural networks was used. The results show effectiveness of the proposed methodology. In fact, we obtained correct classification of 89.3% over testing data set.

KEYWORDS
classification, features extraction, neural networks, pattern recognition

1 | INTRODUCTION

The field of organic materials for energy harvesting and power conversion has encountered a rapid growth in the last decade. On the field of photovoltaics organic solar cells (OSC) have become an attractive technology due to its intrinsic properties such as mechanical flexibility, lightweight, and transparency, as well as the prefigured advantages of low manufacturing costs in the near future.[1-3] In fact, due to its versatility, OSC technology can count on many possible further applications: for example, to realize curved surfaces for smart windows, organic fabrics for photovoltaic clothings, intelligent and self sustained sensors systems, and so on. Moreover, although the power conversion efficiency of an OSC barely exceeded 10% under lab conditions, such a technology opens to wide-scale employment on large surfaces (e.g., for building facades), making up for the apparently low conversion efficiency. This latter is primarily caused by surface defect on the OSC bestowed mainly to the cheap fabrication process. In facts, differently from a traditional photovoltaic cell, an OSC can be produced at low temperatures and does not requires a vacuum chamber or particularly clear environments. Therefore, while the production of an OSC requires lowers the expenses with respect to a traditional silicon-based device, the physical defects introduced on the OSC's structure tampers with its conversion efficiency. These defect could result by many accidents throughout the OSC fabrication process, for instance, by scratches, uneven morphologies, and so on. There are many possible variations of intelligent systems which are trained to detect patterns, extract image features or identify defects on a surface[4-11] However, in general, bulk defects, interface defects, and interconnect defects can generate shunt and series resistance within the cell, contrarily it is yet uncertain the peculiar effect of many kind of defects on the OSC functionality.[12-14] For that reason it is crucial to implement methodologies for detection, localization, and identification of physical defects, not only during the production cycle, but also at design time.

2 | DEVICE OPERATION

Production cost and overall OSC efficiency would benefit greatly if such defect could be predicted and modeled during the research and development stage that leads to the design of a producible OSC device. Moreover, during mass production stages, an defect detection system integrated on the production line would greatly reduce the number of faulty devices. Since such devices are actually rejected and destroyed only at the end of the production cycle, it would also be of paramount importance to further reduce the overall production cost. In this paper we propose an image processing approach, based on elliptical basis function neural networks

(EBFNN), for OSC physical defects detection and identification trough the analysis of microscopy imagery. Such a microscopy imagery has been examined by means of advanced image processing tools as well as characterized analytically by means of Zernike Polynomials. This latter analysis is responsible to provide the device-characteristics data to be correlated by means of EBFNN. The organization of the paper is the following: the Section 2 introduce the argument and the paper scope. The Section 3 provides a brief description of Zernike polynomials, on which the technique of feature extraction is based. The Section 4 report a a short description concerning the neural network that constitutes the adopted classifier and a detaliad explanation of the innovative training procedure on purpose designed by the authors for the neural network. Section 5 describe the case study, while the Section 6 display the obtained results with a discussion on they. Finally in Section 7 the conclusion are drawn.

OSC's physical defects often result in a detrimental effect on its power conversion performances. An OSC converts light into electric power by means of the photovoltaic effect. This effect is achieved when a photon excites an electron which leaps to the conduction band of a semiconductor material and is extracted by means of a small electrical potential. In OSCs the photovoltaic effect takes place into an organic layer. The organic layer of an OSC is generally made by two different organic materials with semiconductor characteristics, an high light-absorption efficiency, as well as considerable conducting properties. The organic materials used in OSC manufacturing usually absorb light constituted by photons within an energy range of 1–3 eV. These corresponds to a large portion of the visible and infrared light spectrum, grossly 400–700 nm, which is basically also the characteristic spectrum of the light coming from the Sun (excluding the ultraviolet radiation). Therefore, in organic photovoltaic technology, the implemented organic materials play the role of electron donors and acceptors. It means that the materials should have the capability of conducting holes and electrons, analogously to n-doped (donors) and p-doped (acceptors) inorganic semiconductors. There are, however, some major differences between organic and inorganic semiconductors, which should be considered when accounting for the OSC operation. One of the main issues with organic materials is their small dielectric constant. This latter leads to the formation of tightly bound excitons due to light absorption. These excitons could reach binding energies greater than 0.3 eV. In this case it will not be possible to dissociate free charge carriers by means of temperature and neither by applying external electric field. Consequently, the mechanism that leads to current generation in OSC differs from inorganic solar cells. Demonstration of the OSC operation principle is shown in Figure 1. First, (a) a photon is absorbed mostly by the donor material and excite an electron to create a coulomb bounded state of electron and hole, also called exciton, rather than free charges. The (b) exciton diffuses towards a donor–acceptor interface to be able to be separated. However, the low diffusion length (approximately 10 nm) requires multiple junctions within the layer; this obtains by blending the donor and acceptor together. As a result, there are spatially distributed junctions throughout the organic layer with phase separation on the order of the diffusion length. Such configuration dramatically increase the efficiency of the cell. Upon encountering a junction, (c) charge transfer by means of an energy exchange between the electrons that are concurrently enabling an exciton bonding to the adjacent molecule. This process results in the formation of a Polarons–Pair (PP) state. This PP state can dissociate into free charge carriers at a certain rate, depending on the temperature and electric filed. After the formation of free charge carriers, it is essential that they will (e) transport toward, and (f) be collected at the correct electrode. The complex morphology necessary for efficient exciton dissociation, drastically impairs the conduction of free charge carriers towards the electrodes. Thus, a very thin layer (approximately 100 nm) is required to

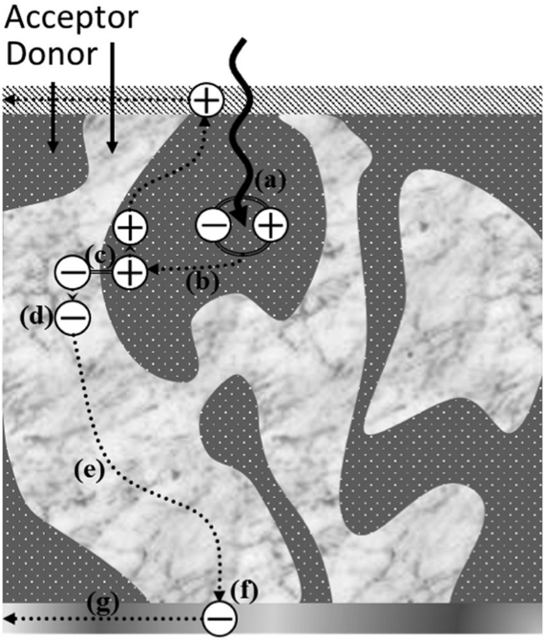

FIGURE 1 The process of current generation in organic solar cells after a photon absorption event (a) that generates an electron-hole pair (b). The pair is thes separated (c) while the electron is preemted by the acceptor (d), transferred (e) and captured by a conductive material (f) in order to be discharged (g) to generate an electrical current

attain an optimized device. Such a thin layer can be easily damaged, therefore even the slightest defect can cause a major drop in performances. Moreover, when a physical defect occurs, it hinders the junction formation. In this eventuality the free charge carrier formation is stemmed, also the path of excitons and free charge carriers is dumped, locally decreasing the material conductivity. As a result, defects promote shunts or discontinuations in the cell due to the low thickness of the layer. In addition, the disordered nature of organic materials can lead to a poor connection between the organic material and the electrodes, hence, increasing the contact resistivity. Detecting defects during the different stages of the fabrication processes can reduce the formation of poor contacts, shunts and low conductive regions and lead to better fabrication technique. As such, dramatically increases OSC performance. Using computational models, we were able to snapshot microscopic images, and automatically detect the defects and correlate them to the electric power of the device. In this study we implements an elliptic basis neural network to identify physical defect by means of a feature extraction preprocessing technique based on the Zernike polynomials. These techniques are introduced in the following.

3 | ZERNIKE'S POLYNOMIALS

Zernike's polynomials functions are a set of two-dimensional orthogonal polynomials defined on a circular domain of unitary radius.[15,16]

$$C = [0, 1] \times [0, 2\pi] \subset \mathbb{R}^2 \tag{1}$$

As a natural consequence of their definition domain, Zernike's polynomials are generally expressed in polar coordinates by means of two variables: a polar phase ϑ and a radial module ϱ. Zernike's polynomial are identified by means of two indexes: a radial index $n \in \mathbb{N}$, and an angular index $m \in \mathbb{Z}$ with

$$\frac{n - |m|}{2} \in \mathbb{N} \tag{2}$$

or, in other words, that $|m| \leq n$ and that $(n - |m|)$ is an even number. Under the condition (2), a Zernike's polynomial $Z_n^m : \mathrm{C} \rightarrow \mathbb{R}$ is representable as

$$Z_n^m(\varrho, \vartheta) = N_n^m \; R_n^{|m|}(\varrho) \, M(m\vartheta) \qquad \begin{array}{l} \forall \;\; n \in \mathbb{N}, \\ \forall \;\; m \in \mathbb{Z}, \\ \forall \;\; (\varrho, \vartheta) \in \mathrm{C}, \end{array} \tag{3}$$

where in Equation (3), at the right side with respect to the equal sign, the three coefficients are respectively: a normalization coefficient N_n^m, a radial parameter $R_n^{|m|}$, and an angular parameter $M(m\vartheta)$. Such parameters are defined as follows.

3.1 | Normalization term N_n^m

$$N_n^m = \sqrt{(2 - \delta_{0,m})(n + 1)} \tag{4}$$

where

$$\delta_{0,m} = \begin{cases} 0 & m \neq 0 \\ 1 & m = 0 \end{cases} \tag{5}$$

3.2 | Radial parameter $R_n^{|m|}$

$$R_n^{|m|}(\varrho) = \sum_{s=0}^{\frac{n-|m|}{2}} \frac{(-1)^s \varrho^{n-2s} (n - s)!}{s!\left(\frac{n+\,|m|}{2} - s\right)!\left(\frac{n-\,|m|}{2} - s\right)!} \tag{6}$$

with $0 < R_n^{|m|}(\varrho) < 1 \quad \forall \quad \varrho \in [0, 1]$.

3.3 | Angular parameter $M(m\vartheta)$

$$M_n^m(m\vartheta) = \begin{cases} \cos(m\vartheta) & m \geq 0 \\ \sin(|m|\vartheta) & m < 0 \end{cases} \tag{7}$$

with $-1 < M_n^m(m\vartheta) < 1 \;\forall\; \vartheta \in [0, 2\pi]$.

Finally, Zernike's polynomials can be of interest for polynomial expansion of a arbitrary wavefronts over a circular aperture of arbitrary radius a so that

$$\varrho = \frac{r}{a}, \tag{8}$$

where r is called radial distance from the central aperture. It follows that Zernike's polynomials are extremely useful when selected as basis for the representation of images.

3.4 | Zernike moments

Given a grayscale image it is possible to apply the Zernike's polynomials as a basis for a multiresolution projective space to represent the image as a set of coefficients called Zernike's moments.[17] The Zernike's moments for a grayscale image $I(x, y)$ can be defined as follows:

$$A_{n,m} = \frac{n+1}{\pi}\sum_x\sum_y I(x,y)V^*_{n,m}(\varrho, \vartheta)\; e^{im\vartheta}, \tag{9}$$

where the indexes n, m represents the moments order, and the $V^*_{n,m}$ represent the conjugate of $V_{n,m}$, given the classical polar coordinate transform

$$\begin{cases} \varrho = \sqrt{x^2 + y^2} \\ \vartheta = \tan^{-1}\dfrac{y}{x} \end{cases} \tag{10}$$

The functions $V_{n,m}$ in (9) are defined as follows:

$$V_{n,m}(\varrho, \vartheta) = R_n^{|m|}(\varrho)\; e^{im\vartheta}. \tag{11}$$

The Zernike's moments have the following properties, suitable for pattern recognition[18]:

1. *Rotation invariance*. The modulus of Zernike's moments is rotational invariant.
2. *Robustness*. Zernike's moments are robust to noise and to small variations in shape.
3. *Information representation efficiency*. Since the Zernike's polynomials are orthogonal, each Zernike's moment specifically represents a unique portion of the information contained on the image. It follows that informational redundancy is avoided.
4. *Effectiveness*. An object can be well described by a small set of related Zernike's moments.

Due to their mathematical structure, such moments are able to efficiently represent the information contained on segmented images. Therefore in this paper we will use Zernike's moment to extract features from scanning electron microscope images. These features will be used to detect the presence of a physical defect on the scanned device by mean of an elliptical basis neural network (Figure 2).

4 | THE NEURAL NETWORK

4.1 | Feed forward neural networks (FFNN)

A FFNN is a directed graph composed of a finite number of nodes, called neurons, and weighted edges, called connections. The neurons are organized in layers: an input layer, an output layer and a variable number of hidden layers. The neurons of each hidden layer are called hidden neurons. This latter uses the output of the previous layer's neurons as an input

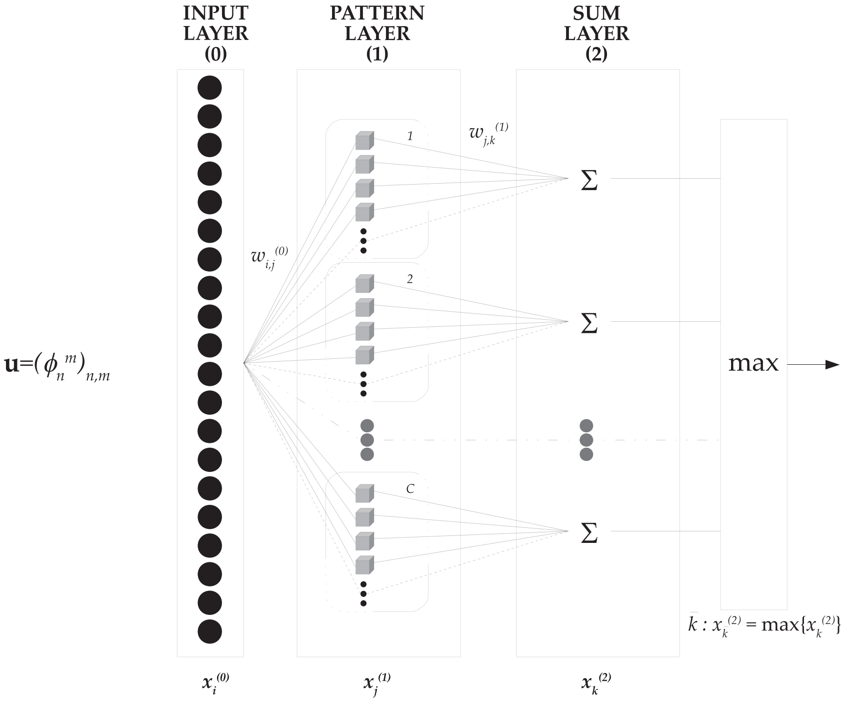

FIGURE 2 The adopted neural network

weighted by means of the related connections' weights, and computes on such input a function (called activation o transfer function). In a general formulation, suppose an N-dimensional input $\mathbf{u} \in \mathbb{R}^N$ so that

$$\mathbf{u} = (u_i)_{i=1}^{N}. \tag{12}$$

Then we will define *input layer* the set of neurons $x_i^{(0)}$ so that the ith neuron, with $i \in [1, N] \cap \mathbb{N}$, can be identified as follows:

$$x_i^{(0)} = u_i \tag{13}$$

with $\mathbf{u} \in \mathbb{R}^N$. Given the lth hidden layer, with $l \in [1,\ L] \cap \mathbb{N}$, supposing it composed of N_l neurons, and given $j \in [1, N_l] \cap \mathbb{N}$, the output of the jth neuron can be similarly formalized as follows:

$$x_j^{(l)} = \gamma_j^{(l)}\left(b_j^{(l)} + \sum_{i=1}^{N_{l-1}} w_{ij}^{(l)} x_i^{(l-1)}\right) \tag{14}$$

where $\gamma_j^{(l)}$ represents its activation function, and $b_j^{(l)}$ is a bias, while N_{l-1} is the number of neurons in the previous layer, and $w_{ij}^{(l)}$ are the connection weight from the ith neuron, with output $x_i^{(l-1)}$, on the $(L-1)$th layer to the jth neuron on the Lth layer. Finally, if the output layer is composed of M neurons, such neurons, with value y_k, given $k \in [1, M] \cap \mathbb{N}$, will be defined as follows:

$$y_k = \gamma_k^{(L)}\left(b_k^{(L)} + \sum_{j=1}^{N_{L-1}} w_{jk}^{(L)} x_j^{(L-1)}\right) \tag{15}$$

so that the output vector $\mathbf{y} \in \mathbb{R}^M$, with $\mathbf{y} = (y_k)_{k=1}^M$, results

$$\mathbf{y} = \mathcal{N}(\mathbf{u}), \tag{16}$$

where $\mathcal{N}$ represents the neural network acting as a function $\mathcal{N} : \mathbb{R}^N \to \mathbb{R}^M$ that associates to each input vector $\mathbf{u}$ an output vector $\mathbf{y}$ computed by means of (13) to (15).

4.2 | Probabilistic neural networks

As well known in literature, FFNN can be opportunely adapted to approximate probability distribution functions as a superposition of Parzen windows,[19] it follows that neural networks topology can be adapted, basing on a derivation of Bayesian network models, to behave as multiclass probabilistic classifier.[20] These networks are called probabilistic neural networks (PNN). The classifier developed in this study is based on a neural network. The idea is that the application of probabilistic theory into the construction of neural network architectures.[21] Such a type of neural network is very efficient when working with a mathematical model that must cover a wide variation of simulated cases of the input object states from prior assumptions. Initial data can be incomplete and therefore an applied methodology must cover all the possible incompleteness within applied processing to provide most accurate decision support at the output.

4.3 | Elliptical basis function neural networks

In this study we have modeled an alternative Feed Forward Probabilistic Neural Network model, called EBFNN, to recognize surface defects from the image representation in terms of Zernike's moments. Similarly to the FFNN topology devised in Section 4, also in the EBFNN topology the input vector $\mathbf{x}^{(0)}$ constitutes the input layer itself, this latter is the input of each neuron on the first hidden layer, that, for historical reason, it is called *pattern layer*, while the component neurons are called *pattern units*).[22] Given a N-dimensional input vector, on an EBFNN, each of the N pattern units composing the pattern layer implements an EBF, therefore the jth unit will compute the following:

$$x_j^{(1)} = e^{-\frac{1}{2}(\mathbf{x}^{(0)}-c_j)^T \hat{\Sigma}_j^{-1} (\mathbf{x}^{(0)}-c_j)} \quad \forall \;\; j \in [1, N] \cap \mathbb{N}, \tag{17}$$

where c_j represents the data centroids associated with the jth pattern unit, and $\hat{\Sigma}_j$ the covariance matrix

$$\hat{\Sigma}_j = (\sigma_{jr})_{j,r=1}^N \tag{18}$$

that determines the directional sensitivity of the jth pattern unit along the input space dimensions (indexed with the number $r \in [1, N] \cap \mathbb{N}$). For the sake of shortness and clarity (17) can be rewritten as follows:

$$x_j^{(1)}(n) = \phi_j(n) \quad \forall \;\; j \in [1, N] \cap \mathbb{N}, \tag{19}$$

where ϕ will be referred as activation. In this latter, n identifies the nth input pattern fed to the network. The training algorithm adjust the neruon's parameters to specialize each unit to recognize a part of the data cluster that composes a class. This permits to refine the

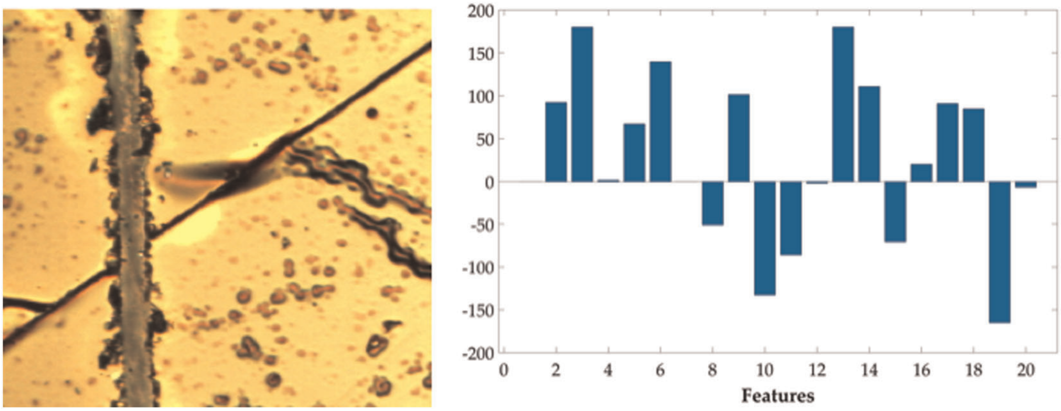

FIGURE 3 Defects on layers consisting of scratches deriving from human interaction such as a coarse handling of the device, as well as by collisions or abrasions due to the fabrication process (left) and its extracted features (right) [Color figure can be viewed at wileyonlinelibrary.com]

classification capability of the neural classifier in terms of Mahalanobis distance.[23,24] Each patter unit's output is the fed to the summation neurons of the summation layer. As well as the pattern layer is fully connected with the input neurons, for the implemented topology, also the summation layer is fully connected with the pattern units. Therefore, given C possible classes, for each one of such classes, the kth summation unit will compute the following:

$$x_k^{(2)} = \sum_{j=1}^{N} w_{jk}\ \mathbf{x}_j^{(1)} \quad \forall\ k \in [1, C] \cap \mathbb{N}, \tag{20}$$

where N is the size of the pattern layer, and w_{jk} is a weight determined during training for each connection between the jth pattern unit and the kth summation unit. Each neuron in the output layer recognize the largest among the received inputs and the source neuron, therefore recognizing the class, so that given (Figures 3 and 4)

$$x^{(3)} = y \in [1, C] \cap \mathbb{N} \tag{21}$$

and with

$$y = \bar{k} : x_{\bar{k}}^{(2)} = \max_{k} \left\{ x_k^{(2)} \right\}. \tag{22}$$

5 | EBFNN NETWORK TRAINING

The implemented EBFNN has been trained by means of a modified backpropagation algorithm. Defined a vector $\mathbf{t}(n)$ of target probabilities

$$\mathbf{t}(n) = (\delta_{kc(n)})_{k=1}^{C} \quad \forall\ n \in [1, P] \cap \mathbb{N} \tag{23}$$

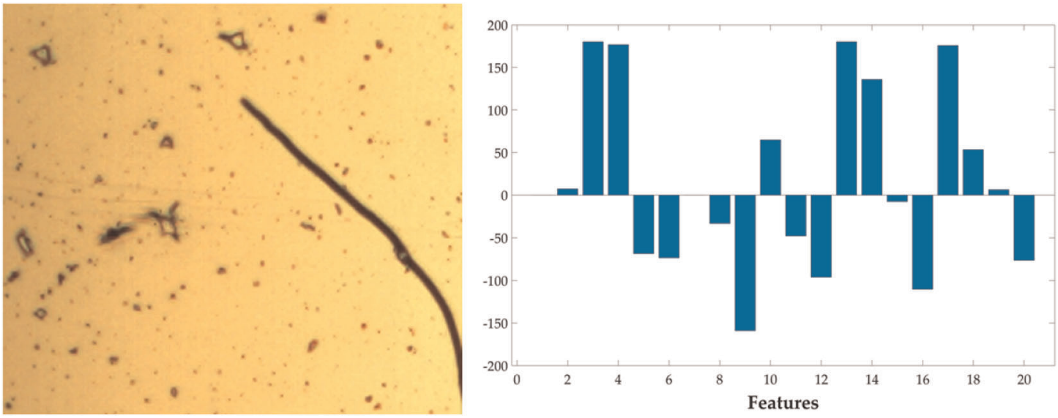

FIGURE 4 Defects due to visible fractures or fatigue striations aluminum surfaces of a device sample, randomly choosen (left) and its extracted features (right) [Color figure can be viewed at wileyonlinelibrary.com]

where $c(n)$ identifies the class associated to the nth input training vector $\mathbf{p}(n)$ among a total of P different patterns used to train the network. At each training step the network error is computed as follows:

$$\epsilon = \frac{1}{2}\sum_{n=1}^{P}\sum_{k=1}^{C} e_k^2(n) = \frac{1}{2}\sum_{n=1}^{P}\sum_{k=1}^{C}\left[x_k^{(2)}(n) - t_k(n)\right]^2 \tag{24}$$

where n is the training pattern index, and P the total number of training patter, to be classified in one of the C classes. Basing on the MSE $\epsilon(\tau)$, computed at the τth training step, the weights the summation layer are updated so that

$$w_{jk}(\tau+1) = w_{jk}(\tau) - \eta_w \frac{\partial \epsilon(\tau)}{\partial w_{jk}(\tau)} \tag{25}$$

where η_w is a weights related learning rate parameter. It follows that, by applying the Chain Rule method,[25] it is possible to consequently update the EFBNN parameters as follows:

- Network centroids

$$\Delta c_{jr}(\tau) = \eta_c \sum_{k=1}^{C} \frac{e_k^2(n)\phi_j(n)\left[x_k^{(0)}(n) - c_{ij}\right]^2}{\sigma_{jr}^3(\tau)}, \tag{26}$$

  where η_c is a centroids related learning rate parameter so that $c_{jr}(\tau+1) = c_{jr}(\tau) + \Delta c_{jr}(\tau)$;
- Network spreads

$$\Delta \sigma_{jr}(\tau) = \eta_\sigma \sum_{k=1}^{C} \frac{e_k^2(n)\phi_j(n)\left[x_k^{(0)}(n) - c_{ij}\right]^2}{\sigma_{jr}^3(\tau)} \tag{27}$$

  where η_σ is a sigma related learning rate parameter so that $\sigma_{jr}(\tau+1) = \sigma_{jr}(\tau) + \Delta \sigma_{jr}(\tau)$;
- Network weights

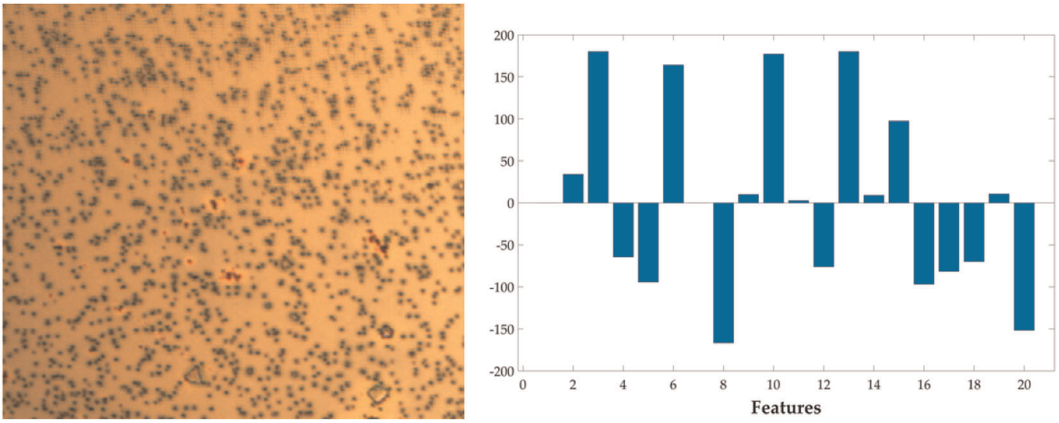

FIGURE 5 Defects characterized by presence of multiple voids, grains, or spots caused by high level of environmental humidity or unwanted contact with water particles that intrude the compound (left) and its extracted features (right) [Color figure can be viewed at wileyonlinelibrary.com]

$$\Delta w_{jk}(\tau) = \eta_w \sum_{k=1}^{C} e_k^2(n)\phi_j(n) \tag{28}$$

so that $w_{jk}(\tau + 1) = w_{jk}(\tau) + \Delta w_{jk}(\tau)$.

Contrarily, a fast and specific training must take advantage of several pruning steps that as explained in the following sections (Figures 5 and 6).

6 | EBFNN ADAPTIVE PRUNING

In literature[26-28] there are several known approaches for pruning algorithms and their implementation. Unfortunately a classical approach to the pruning phase could seriously tamper with the overall performances of the classifiers.[29,30] In this study, we needed to develop a more

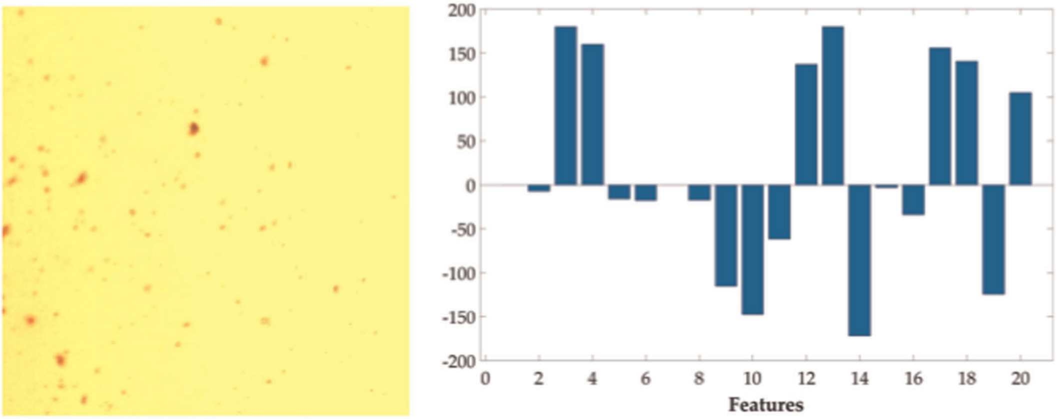

FIGURE 6 Surface morphology of a not defective device sample, randomly choosen (left) and its extracted features (right) [Color figure can be viewed at wileyonlinelibrary.com]

customized approach for pruning due to the intrinsic nature of the data patterns. We developed a pruning method that considers the overall weight matrix for each layer of the network after each training phase, and extrapolates several centroids on the weights space by means of the *k*-means algorithm. Subsequently, partitioning the said weights space, it is possible to exclusively prune the partition with the lower score on the partitioning algorithm. The procedure can be described in nine steps:

1. Create a random distribution of centroids;
2. Partition the weights space in centroids' classes;
3. Attribute class memberships to the weights;
4. Recompute the centroids and classes;
5. Continue until convergence;
6. Detect the weights' partition to prune;
7. Prune the related pattern layer units;
8. Re-evalutate network's error;
9. Add centroids and iterate until stop conditions.

The said steps are now described. Starting from the devised neural network (15), and, namely, regarding the pattern layer $\bar{l}$, let $W_{\bar{l}}$ be its weights matrix. It follows:

$$W_{\bar{l}} = \left\{ w_{ij}^{(\bar{l})} \ \ \forall \ \ i \in \left[1, N_{\bar{l}-1}\right] \cap \mathbb{N}, \ \ \forall \ \ j \in [1, N_{\bar{l}}] \cap \mathbb{N}, \} \subset \mathbb{R}. \right. \tag{29}$$

Let now define a metric function $\delta: \mathbb{R} \rightarrow \mathbb{R}$

$$\delta(x_1, x_2) = || x_1 - x_2 ||^2 \quad \forall \ \ x_1, x_2 \in \mathbb{R}. \tag{30}$$

Then, for the nth iteration of the overall procedure, given a set $C_n^{\bar{l}}$ of centroids in $[\min(W_{\bar{l}}), \max(W_{\bar{l}})]$, randomly distributed at the first, and starting with a user-defined size N_c so that $|C_n^{\bar{l}}| = N_c$, we can define, at each time step τ_n, a membership function $\mu: W_{\bar{l}} \rightarrow C_n^{\bar{l}}$ computed for each weight as follows:

$$\mu\left(w_{ij}^{(\bar{l})}\right) = \bar{c}_n^{\bar{l}}(\tau_n) \tag{31}$$

so that

$$\delta\left(w_{ij}^{(\bar{l})}, \bar{c}_n^{\bar{l}}(\tau_n)\right) = \min_{C_n^{\bar{l}}}\left\{\delta\left(w_{ij}^{(\bar{l})}, c_n^{\bar{l}}(\tau_n)\right)\right\}. \tag{32}$$

It follow that during the time step τ_n, the weight $w_{ij}^{(\bar{l})}$ is assigned to the centroid $\bar{c}_n^{\bar{l}}(\tau_n)$. For each centroid, at each time step τ_n, it is possible to define centroid-related classes

$$\mathrm{C}\left[c_n^{\bar{l}}(\tau_n)\right] = \left\{w_{ij}^{(\bar{l})} \in W_{\bar{l}}: \mu\left(w_{ij}^{(\bar{l})}\right) = c_n^{\bar{l}}(\tau_n)\right\} \quad \forall \ \ c_n^{\bar{l}}(\tau_n) \in C_n^{\bar{l}}. \tag{33}$$

Based on the latter, before each time-step $\tau_n > 1$, the new centroids $c^{\bar{l}}(\tau_n)$ are recomputed as follows:

$$c_n^{\bar{l}}(\tau_n) = \frac{\sum_{\mathrm{C}\left[c_n^{\bar{l}}(\tau_n-1)\right]} w_{ij}^{(\bar{l})}}{\left|\mathrm{C}\left[c_n^{\bar{l}}(\tau_n - 1)\right]\right|}. \tag{34}$$

Therefore the new centroids will be positioned to the average weight in the class $C[c_n^{\bar{l}}(\tau - 1)]$, where $c_n^{\bar{l}}(\tau_n - 1)$ are the old centroid and $C[c_n^{\bar{l}}(\tau_n - 1)]$ the old classes. Once the new centroids have been computed, for each weight in $W_{\bar{l}}$ a new membership function is evaluated as in (31), and consequently the new classes $C[c_n^{\bar{l}}(\tau_n)]$ are composed. The process is iterated until convergence of the k-means algorithm. After k-means convergence, we can consider concluded the centroid and classes evaluation for the current iteration. Let call n the iteration index, then, after the k-means algorithm returned, at a time step $\bar{\tau}_n$, we can select the minimum centroid $\chi_n^{\bar{l}}$ at the nth iteration as follows:

$$\chi_n^{\bar{l}} = \min\left\{\left|c_n^{\bar{l}}(\bar{\tau}_n)\right|\right\}. \tag{35}$$

Finally, basing on (35), a tentative pruning is performed by removing each weight $w_{ij}^{(\bar{l})} \in C[\chi_n^{\bar{l}}]$, and therefore, by pruning the relative network connection. The pruning procedure, is then performed backwardly, for each layer, in a similar fashion. After the nth iteration of the overall layer-by-layer pruning procedure, the neural network is retrained and tested. The performances variation is computed as

$$\Delta_n = |E_n - E_{n-1}|, \tag{36}$$

where E_n is the network error after the nth overall pruning iteration, and E_{n-1} the network error at the end of the previous iteration (or before the overall procedure for $n = 1$). Finally the nth overall iteration is positively evaluated if

$$\begin{cases} \frac{\Delta_n}{\Delta_{n-1}} < \vartheta, \\ E_n < \varepsilon, \end{cases} \tag{37}$$

where ϑ and ε are two user-defined thresholds, respectively, representing the maximum relative performance variation and the maximum network error allowed. If the last iteration is not evaluated positively, then next iteration $(n + 1)$ is computed. The procedure continues until it reaches a positive evaluation or an user-defined iteration limit Figure 7.

7 | CASE STUDY

The presented model has been applied to a scanning electron microscope (SEM) images data set collected at the Rafi Shikler's laboratory within the the Department of Electrical and Computer Engineering at the Ben Gurion University of the Negev. OPV's defects manifest themselves as a variation of the image texture. These images have been gathered experimentally on real OPV cells, moreover the an extensive campaign of simulations showed that Zernike's moments phases reach good performances as image descriptors. In facts the phases of Zernike's moments, extracted as shown in Section 3, efficiently capture the texture variations related to the presence of physical defects.

7.1 | Device fabrication

For the purpose of defect detection, we have fabricated a series of solar cells using spin-coating technique. The cell is made up from several layers stack upon each other. First is the

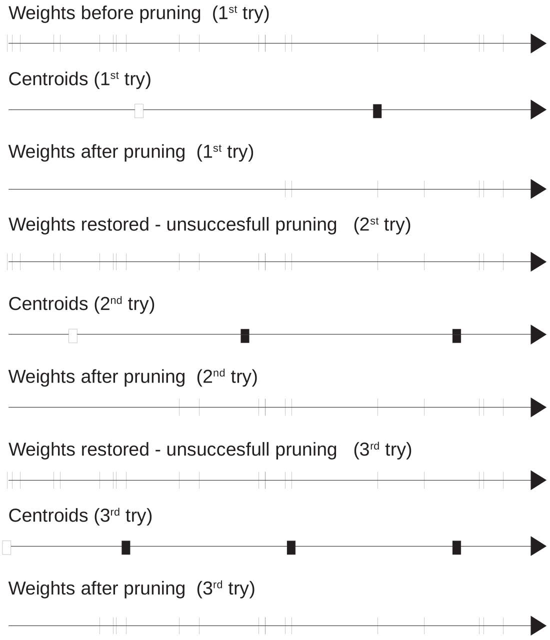
Weights before pruning (1st try)
Centroids (1st try)
Weights after pruning (1st try)
Weights restored - unsuccesfull pruning (2st try)
Centroids (2nd try)
Weights after pruning (2nd try)
Weights restored - unsuccesfull pruning (3rd try)
Centroids (3rd try)
Weights after pruning (3rd try)

FIGURE 7 A graphical representation of theli pruning procedure

transparent substrate, the other layers follow the order of a transparent anode, a Hole Transport Layer or HTL, an active layer (the organic layer) and last is the cathode. The substrate made from 0.7 mm thickness glass with an area of 12 × 12 mm. The anode is predeposited on top of the substrate by the manufacturer; it is a 90 ± 10 nm layer of indium tin oxide (ITO) with an area of $6 \times 12\,\mathrm{mm}^2$ and a resistivity of $20\,\mathrm{Ohm/m}^2$. Before the fabrication process, in the laboratory fume hoods the glass + ITO substrate was cleaned by an ultrasonic bath with acetone, methanol, and isopropanol for 15 min each; next, it was treated with UV-ozone for 4 min. Over the glass + ITO we have spin-coated at 5000 RPM to produce a 30 nm layer of the HTL. The HTL is made from the polymer poly(3,4-ethylenedioxythiophene)-poly (styrenesulfonate) (PEDOT:PSS). This transparent and conducting conjugated polymer aid the transportation of holes from the active layer into the anode. The rest of the process has been made inside a glove-box to provide an inert atmosphere. Since PEDOT:PSS is highly hydrophile, it has been dried on a hot plat at 105°C for an hour to remove excess water. Upon the PEDOT:PSS we have spin-coated at 1000 RPM the active layer. The active layer is made from solution blend of [6,6]-phenyl C61 butyric acid methyl ester (PCBM) and poly(3-hexylthiophene-2,5-diyl) (P3HT) dissolved in chloroform. The solution is 1:1 wt/wt ratio and has 20 mg/ml. The cathode, made from aluminum, was thermally evaporated through a patterned mask that provided eight finger like contacts as shown in Figure 8 with thickness of 80 nm. Afterward the whole sample was annealed at 140°C for 20 min. for a gentle approach to the finger contacts and ITO with external probes we used a conductive epoxy. To approach the ITO we have screeched the active layer with a toothpick before putting the conductive epoxy. The degradation mechanisms of the active inter-layers involved the diffusion of the molecular oxygen and the water into the device induce chemical reactions in polymer materials, degradation of interfaces, electrode reaction with the organic materials, morphological changes. These modifications give rise to a number of defects in the OPVs. For the recognition of texture

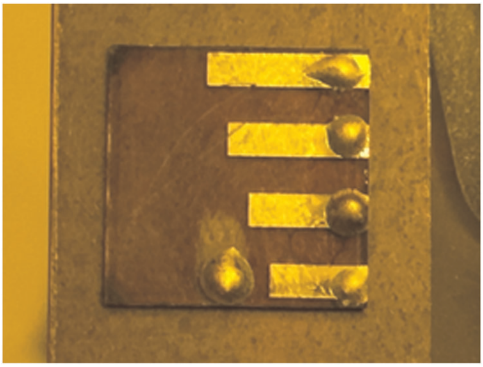

FIGURE 8 A device containing four organic solar cells [Color figure can be viewed at wileyonlinelibrary.com]

variations in the SEM images caused by these defects is crucial the definition of a set of features for texture representation. There are many different modes of representing texture variations, and each is suitable to certain tasks. A feature set suitable for the classification should possess two important properties: should be insensitive to significant translations, and should be have a very low correlation (both interclass that intraclass). The shape feature extracted and described by the Zernike moments is not sensitive to the noises and the values of the Zernike moments are hardly redundant because the kernel of the Zernike moment is the set of the orthogonal radial polynomials. Moreover the low-order Zernike moments can represent the whole shape of the image and the high-order Zernike moments can describe the detail. So, in our case, the shape feature of the image can be represented by a set of the values of the Zernike moments.

7.2 | Image acquisition and feature extraction

The images acquisition is performed with a microscope camera DeltaPix, model *DpxViewPro 1.14.8* (see Figure 9). Microscopy was used to capture the various defects the surface

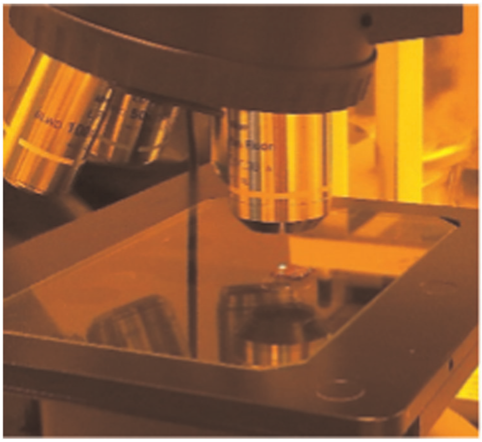

FIGURE 9 The microscope used to identify the organic solar cells defects [Color figure can be viewed at wileyonlinelibrary.com]

morphology on the top of the examined OSCs. The size of the captured images is 1280 × 1024 with an high spatial and color resolution. Some devices analyzed are not defective, others with various kind of defects. The collected images set acquired from the microscopy are grouped in classes each one represents one type of defect analyzed in this paper:

1. Defects on layers consisting of scratches caused by mechanical damage or fabrication during the handling and preparation;
2. Defects due to visible fractures or fatigue striations aluminum surfaces due to original manufacturing crack exposed to high temperatures;
3. Defects characterized by presence of multiple voids, grains, shiny spots and bubbles due to the water infiltration and exposition to high humidity air;
4. Not defective devices.

After a thorough analysis we determined that, to reach an optimal trade-off among the representation's accuracy and the required computational complexity, it is safe to represent the SEM images as a set of twenty Zernike's moments of increasing order from 0 to 7. Finally, it has been shown that the phase of such Zernike's moment suffices to discriminate the different kind of defects, and that any other information on the image colors are unnecessary. It follows that, each image has been represented as a features vector composed of the phases o the Zernike's moment extracted from grayscale SEM images. Therefore we have acquired 93 images for each class. Thus the obtained data set contains 372 images. For each image we have then extracted a features vector

$$\mathbf{u} = \left(\varphi_n^m\right)_{n,m} : \begin{cases} n = 0, & m = 0 \\ n = 1, & m = 1 \\ n = 2, & m \in \{0, 2\} \\ n = 3, & m \in \{1, 3\} \\ n = 4, & m \in \{0, 2, 4\} \\ n = 5, & m \in \{1, 3, 5\} \\ n = 6, & m \in \{0, 2, 4, 6\} \\ n = 7, & m \in \{1, 3, 4, 5\} \end{cases} \tag{38}$$

where φ_n^m identifies the phase of the Zernike's moment Z_n^m (see Table 1). The Figures 3–6 show a marked difference between features belonging to the different classes of devices. Then this feature set proves extremely suitable for the problem classification addressed in this paper.

8 | RESULTS AND DISCUSSION

The proposed architecture has been tested using the features vectors extracted from the images acquired as described in Section 7. The feature vector, which is used as input for the neural classifier, namely x_n^0, can be defined as follows:

$$\mathbf{x}_n^{(0)} = \mathbf{u}(n) \quad \forall \ n \in [1, N] \cap \mathbb{N} \tag{39}$$

where $\mathbf{u}(n)$ identifies the feature vector, as in (38), for the nth acquired image. The neural network was then trained to classify the input data in the four different classes (see Table 2). The training set composed of 316 samples (79 samples for each class), therefore the number of

TABLE 1 List of Zernike moments used for defects description

n	Moments	Number of moments
0	Z_0^0	1
1	Z_1^1	1
2	Z_2^0, Z_2^1	2
3	Z_3^1, Z_3^3	2
4	Z_4^0, Z_4^2, Z_4^4	3
5	Z_5^1, Z_5^3, Z_5^5	3
6	Z_6^0, Z_6^2, $Z_6^4 Z_6^6$	4
7	Z_7^1, Z_7^3, $Z_7^5 Z_7^7$	4

TABLE 2 The table reports, for each class, the total number of collected samples (N), as well as the number of samples used as training patterns N_P and test N_T

CLASS		*N*	N_P	N_T
1	Scratches	93	79	14
2	Cracks	93	79	14
3	Spots	93	79	14
4	Normal	93	79	14
	Total	372	316	56

pattern unit of the EBFNN was 316, accordingly to the maximum number of possible patterns. Finally, accordingly to the number of classes, the summation layer was composed of four units, while the neural network was provided with one output neuron as maximum selector. During the training phase the neural network has been validated by means of other 56 samples (14 for each class), differing from the training samples. At the end of the training sequence the network has been finalized with 187 pattern units. The evaluation of the proposed method was carried out by using a test vector of new data (unknown to the neural network) composed of 56 samples (14 for each class), differing from the validation set although in similar number. The classification results as been reported in a confusion matrix ($\hat{Z}$).[31] The confusion matrix, reported in Figure 10, reports the number of samples truly belonging to the different target classes (rows) were predicted to belong to that the same output class (columns). Therefore a sample belonging to the target class t_i that has been predicted to belong to the output class o_j is reported as Z_{ij} so that

$$\hat{Z} = (Z_{ij}) = \sum_{i=1}^{C} \sum_{j=1}^{C} t_i \wedge o_j \tag{40}$$

where $r_i \wedge p_j$ is the boolean AND only when the target class t_i and the o_j are both *true* for the same sample. Starting from the confusion matrix, the evaluation of the proposed method was carried out by using the following statistical classification functions of *sensitivity* ($SEN(\alpha)$) also

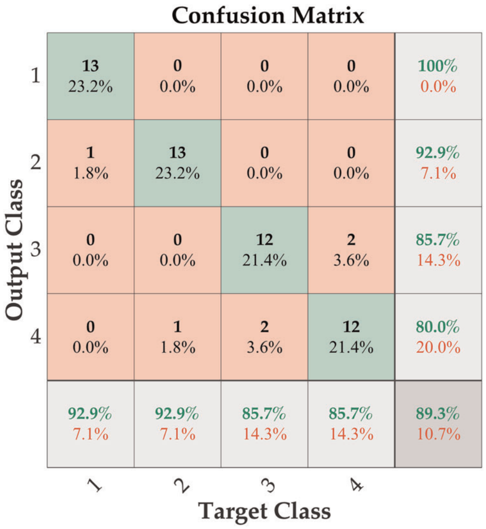

Confusion Matrix

Output Class \ Target Class	1	2	3	4	
1	13 23.2%	0 0.0%	0 0.0%	0 0.0%	100% 0.0%
2	1 1.8%	13 23.2%	0 0.0%	0 0.0%	92.9% 7.1%
3	0 0.0%	0 0.0%	12 21.4%	2 3.6%	85.7% 14.3%
4	0 0.0%	1 1.8%	2 3.6%	12 21.4%	80.0% 20.0%
	92.9% 7.1%	92.9% 7.1%	85.7% 14.3%	85.7% 14.3%	89.3% 10.7%

FIGURE 10 The 4 × 4 confusion matrix obtained analyzing the test set for the four classes (see Table 2). The fifth (light-gray) column reports the class-related sensitivity *SEN* (α), while the fifth (light-gray) row represents the class-related precision *PRE* (α). Finally the last (dark-gray) cell reckons the overall precision and sensitivity. All data are reported in absolute and percentage relative value (black), or in percentage and percentile (green and red) [Color figure can be viewed at wileyonlinelibrary.com]

known as true positive ratio, *specificity* (*SPC* (α)) also known as true-negative ratio, *precision* (*PRE* (α)) also known as positive predictive value, and the negative predictive value (*NPV* (α)), as in Reference [32] so that, given the αth of the C classes, it follows:

$$\mathrm{SNS}(\alpha) = \frac{Z_{\alpha\alpha}}{\sum_{\beta} Z_{\alpha\beta}}, \tag{41}$$

$$\mathrm{SPC}(\alpha) = \frac{\sum_{\beta\neq\alpha}\sum_{\gamma\neq\alpha} Z_{\beta\gamma}}{\sum_{\beta\neq\alpha}\sum_{\gamma} Z_{\beta\gamma}}, \tag{42}$$

$$\mathrm{PRE}(\alpha) = \frac{Z_{\alpha\alpha}}{\sum_{\beta} Z_{\beta\alpha}}, \tag{43}$$

$$\mathrm{NPV}(\alpha) = \frac{\sum_{\beta\neq\alpha}\sum_{\gamma\neq\alpha} Z_{\beta\gamma}}{\sum_{\beta}\sum_{\gamma\neq\alpha} Z_{\beta\gamma}}. \tag{44}$$

Moreover, we computed the overall sensitivity (SNS), which also has the statistical meaning of an overall precision, specificity (SPS), and negative predictive value (NPV), as follows:

$$\mathrm{SNS} = \mathrm{PRE} = \frac{1}{C}\sum_{\alpha}\mathrm{SNS}(\alpha) = \frac{1}{C}\sum_{\alpha}\mathrm{PRE}(\alpha), \tag{45}$$

$$\mathrm{SPC} = \frac{1}{C}\sum_{\alpha}\mathrm{SPC}(\alpha), \tag{46}$$

TABLE 3 The table shows the, given the αth class, the related sensitivity (*SEN* (α)), specificity (*SPC* (α)), precision (*PRE* (α)), and negative predictive value (*NPV* (α)). Finally it is also reported the overall values of accuracy (*ACC*), sensitivity (*SNS*), specificity (*SPC*), precision (*PRE*) and negative predictive value (*NPV*)

α	*SNS* (α) (%)	*SPC* (α) (%)	*PRE* (α) (%)	*NPV* (α) (%)
1	100	~92.86	~92.86	~97.62
2	~92.9	~92.86	~92.86	~97.62
3	~85.7	~85.71	~85.71	~95.24
4	~80.0	~85.71	~85.71	~95.24
ACC	***SNS***	***SPC***	***PRE***	***NPV***
~89.3%	~89.3%	~89.3%	~89.3%	~96.4%

$$\mathrm{NPV} = \frac{1}{C}\sum_{\alpha}\mathrm{NPV}(\alpha). \tag{47}$$

Finally, the overall accuracy (ACC) has been computed as follows:

$$\mathrm{ACC} = \frac{\sum_{\beta} Z_{\beta\beta}}{\sum_{\beta}\sum_{\gamma} Z_{\beta\gamma}}. \tag{48}$$

The obtained measures are reported in Table 3. Based on the statistical meaning of such measures, the sensitivity indicates the percentage of images recordings belonging to a specific category correctly classified, while specificity measures how much the classifier is able to

TABLE 4 The table shows a comparison between our method and different well known methods reported in literature. The methods are enlisted by rows, while the columns reports the related accuracy accuracy (*ACC*), precision (*PRE*), and sensitivity

	ACC (%)	*PRE* (%)	*SNS* (%)
NDF[33]	90	79	82
ABC[33]	90	78	81
IRA[33]	87	75	73
BIP[33]	89	78	80
LDA[34]	84	75	93
QDA[34]	83	71	97
k-NN[34]	86	80	98
SVM-ART[34]	88	80	97
SVM-FD[34]	69	43	97
SVM-GFD[34]	71	49	95
RCF[34]	77	59	96
CVM[35]	N.A.	86	70
Our method	89	89	89

classify the images not belonging to that category. Finally the accuracy provides an indicator of the classifier capability to correctly classify all categories. Basing on this latter we compared our work with several other approaches in literature, as it is shown in Table 4. Namely we compared our precision with several processes that aims to identify surface defects or textural aberration on surfaces. To allow for a fair comparisons, the latter have been restricted only to approaches at least partially comparable, for complexity and outcome, with our work. It is possible to observe that our method generally outperforms the existing method. While some approaches outperform the presented method's sensitivity, on the other hand this result is reached by sacrificing accuracy and precision. Differently, our model is able to maintain an acceptable overall performance among different measurements (accuracy, precision, and sensitivity).

9 | CONCLUSIONS

In this study we presented a new approach for detecting and classifying different types of defects that can occur in the OSC's fabrication process. The proposed approach use the Zernike's moments to extract the features from the scanning electron microscope images and an EBFNN for classifier the different types of defects. To training the neural network and to validate the presented model we have has used a SEM images data set collected at the Rafi Shikler's laboratory within the Department of Electrical and Computer Engineering at the Ben Gurion University of the Negev. The images acquisition is performed with a microscope camera DeltaPix, model DpxViewPro 1.14.8. The size of the captured images is 1280×1024 with an high spatial and color resolution. Some devices analyzed are not defective, others with various kind of defects. The analysis of the results show the effectiveness of the proposed methodology. In fact, the overall values of accuracy is 89%, the sensitivity is 89.3%, the specificity is 89.3%, the precision is 89.3%, and negative predictive value 96.4%.

ORCID

Grazia Lo Sciuto https://orcid.org/0000-0001-9384-7232
Giacomo Capizzi https://orcid.org/0000-0003-2555-9866
Rafi Shikler https://orcid.org/0000-0001-6603-472X
Christian Napoli https://orcid.org/0000-0002-3336-5853

REFERENCES

1. Brabec CJ, Dyakonov V, Parisi J, Sariciftci NS. *Organic Photovoltaics: Concepts and Realization*. Vol 60. Berlin, Heidelberg: Springer Science & Business Media; 2013.
2. Dresselhaus M, Thomas I. Alternative energy technologies. *Nature.* 2001;414(6861):332.
3. Zhao W, Li S, Yao H, et al. Molecular optimization enables over 13% efficiency in organic solar cells. *J Am Chem Soc.* 2017;139(21):7148-7151.
4. Yan C, Gong B, Wei Y, Gao Y. Deep multi-view enhancement hashing for image retrieval. *IEEE Trans Pattern Anal Mach Intell.* 2020:(Early Access). http://doi.org/10.1109/tpami.2020.2975798
5. Yan C, Shao B, Zhao H, Ning R, Zhang Y, Xu F. 3D room layout estimation from a single rgb image. *IEEE Trans Multimedia.* 2020;22(11):3014-3024.
6. Yan C, Li Z, Zhang Y, Liu Y, Ji X, Zhang Y. Depth image denoising using nuclear norm and learning graph model. *ACM Trans Multimedia Comput Commun Appl.* 2021;16(4):1-17.
7. Daniel J, Abudhahir A, Paulin JJ. Tsallis entropy segmentation and shape feature-based classification of defects in the simulated magnetic flux leakage images of steam generator tubes. *Int J Pattern Recognition Artif Intell.* 2020;34(1):2054002.

8. Du B, He Y He Y Duan J, Zhang Y. Intelligent classification of silicon photovoltaic cell defects based on Eddy current thermography and convolution neural network. *IEEE Trans Industr Inform.* 2019;16(10): 6242-6251.
9. Balzategui J, Eciolaza L, Arana-Arexolaleiba N, et al. Semi-Automatic Quality Inspection of Solar Cell based on Convolutional Neural Networks. In: *2019 24th IEEE International Conference on Emerging Technologies and Factory Automation (ETFA)*, Zaragoza, Spain. 2019:529-535.
10. Sun X, Gong S, Han G, Wang M, Jin A. Pruning Elman neural network and its application in bolt defects classification. *Int J Mach Learn Cybern.* 2019;10(7):1847-1862.
11. Su B, Chen H, Zhu Y, Liu W, Liu K. Classification of manufacturing defects in multicrystalline solar cells with novel feature descriptor. *IEEE Trans Instrum Meas.* 2019;68(12):4675-4688.
12. Capizzi G, LoSciuto G, Napoli C, Shikler R, Woźniak M. Optimizing the organic solar cell manufacturing process by means of AFM measurements and neural networks. *Energies.* 2018;11(5):1221.
13. Mittal P, Negi Y, Singh R. analysis for different structures of organic thin film transistors: Modeling of performance limiting issues. *Microelectr Eng.* 2016;150:7-18.
14. Capizzi G, LoSciuto G, Napoli C, Tramontana E. A multithread nested neural network architecture to model surface plasmon polaritons propagation. *Micromachines.* 2016;7(7):110.
15. Lakshminarayanan V, Fleck A. Zernike polynomials: a guide. *J Modern Optics.* 2011;58(7):545-561.
16. Aharmim B, Amal EH, Fouzia EW, Ghanmi A. Generalized Zernike polynomials: operational formulae and generating functions. *Integral Transf Spec Funct.* 2015;26(6):395-410.
17. Chen Z, Sun SK. A Zernike moment phase-based descriptor for local image representation and matching. *IEEE Trans Image Process.* 2010;19(1):205-219.
18. Ryu SJ, Kirchner M, Lee MJ, Lee HK. Rotation invariant localization of duplicated image regions based on Zernike moments. *IEEE Trans Inform Forensics Security.* 2013;8(8):1355-1370.
19. Gupta M, Jin L, Homma N. *Static and Dynamic Neural Networks: From Fundamentals to Advanced Theory*. Hoboken, NJ: John Wiley & Sons; 2004.
20. Specht DF. Probabilistic neural networks. *Neural Networks.* 1990;3(1):109-118.
21. Testolin A, Zorzi M. Probabilistic models and generative neural networks: Towards an unified framework for modeling normal and impaired neurocognitive functions. *Frontier Computat Neurosci.* 2016;10:73.
22. Peng HW, Lee SJ, Lee CH. An oblique elliptical basis function network approach for supervised learning applications. *Appl Soft Comput.* 2017;60:552-563.
23. Mak MW, Kung SY. Kung SY. Estimation of elliptical basis function parameters by the EM algorithm with application to speaker verification. *IEEE Trans Neural Network.* 2000;11(4):961-969.
24. Zhou S, Wang Q, Fang Y, Liu Q. An extreme learning machine method for multi-classification with mahalanobis distance. In: *Proceedings of IEEE*. 2018:35-39.
25. Clark JM, Cordero F, Cottrill J, et al. Constructing a schema: the case of the chain rule? *J Math Behav.* 1997; 16(4):345-364.
26. Hassibi B, Stork DG. Second order derivatives for network pruning: optimal brain surgeon. In: *NeurIPS Proceedings*. 1993:164-171.
27. Huang GB, Saratchandran P, Sundararajan N. A generalized growing and pruning RBF (GGAP-RBF) neural network for function approximation. *IEEE Trans Neural Networks.* 2005;16(1):57-67.
28. Han S, Pool J, Tran J, Dally W. Learning both weights and connections for efficient neural network. In: *NeurIPS Proceedings*. 2015:1135-1143.
29. Passalis N, Tefas A. Dimensionality reduction using similarity-induced embeddings. *IEEE Trans Neural Networks Learn Syst.* 2018;29(8):3429-3441.
30. Hayashi H, Shibanoki T, Shima K, Kurita Y, Tsuji T. A recurrent probabilistic neural network with dimensionality reduction based on time-series discriminant component analysis. *IEEE Trans Neural Network Learn Syst.* 2015;26(12):3021-3033.
31. Fawcett T. An introduction to ROC analysis. *Pattern Recognition Lett.* 2006;27(8):861-874.
32. Beleites C, Salzer R, Sergo V. Validation of soft classification models using partial class memberships: an extended concept of sensitivity & co. applied to grading of astrocytoma tissues. *Chemometrics Intelligent Laboratory Syst.* 2013;122:12-22.

33. Park Y, Kweon IS. Ambiguous surface defect image classification of AMOLED displays in smartphones. *IEEE Trans Industrial Inform.* 2016;12(2):597-607.
34. Anwar SA, Abdullah MZ. Micro-crack detection of multicrystalline solar cells featuring shape analysis and support vector machines. IEEE. 2012:143-48.
35. Qian X, Zhang H, Zhang H, et al. Solar cell surface defects detection based on computer vision. *Int J Performability Eng.* 2017;13(7).

How to cite this article: Lo Sciuto G, Capizzi G, Shikler R, Napoli C. Organic solar cells defects classification by using a new feature extraction algorithm and an EBNN with an innovative pruning algorithm. *Int J Intell Syst*. 2021;1–22. https://doi.org/10.1002/int.22386